

Research Article

Improved Delay-and-Sum Beamforming Algorithm for Breast Cancer Detection

M. Klemm, I. J. Craddock, J. A. Leendertz, A. Preece, and R. Benjamin

*Centre for Communications Research, Department of Electrical and Electronic Engineering,
University of Bristol, Woodland Road, Bristol BS8 1UB, UK*

Correspondence should be addressed to M. Klemm, m.klemm@bristol.ac.uk

Received 4 October 2007; Accepted 3 April 2008

Recommended by Elise Fear

We have evaluated a modified delay-and-sum (DAS) beamforming algorithm for breast cancer detection with a microwave radar-based system. The improved DAS algorithm uses an additional weight factor calculated at each focal point to improve image quality. These weights essentially represent the quality of preprocessing and coherent radar operation. Using a multistatic UWB radar system based on a hemispherical antenna array, we present experimental detection of 7 mm and 10 mm phantom tumours. We show that the new proposed DAS algorithm improves signal-to-clutter ratio in focused images by 2.65 dB for 10 mm tumour, and by 4.4 dB for 7 mm tumour.

Copyright © 2008 M. Klemm et al. This is an open access article distributed under the Creative Commons Attribution License, which permits unrestricted use, distribution, and reproduction in any medium, provided the original work is properly cited.

1. INTRODUCTION

X-ray mammography is currently the most common technique used in breast cancer screening. It employs ionising radiation, requires uncomfortable compression of the breast during the examination, and is of limited value for younger women. These limitations of mammography have resulted in research into alternative methods for imaging breast cancer.

Microwave radar-based imaging [1] is one of the more promising candidates and has attracted the interest of a number of research groups around the world.

In radar-based imaging, the goal is to create a map of microwave scattering, arising from the contrast in dielectric properties within the breast. The radar approach originates from military and ground-penetrating applications, and was proposed for breast cancer detection in the late nineties independently by Benjamin in 1996 [2] and Hagness et al. in 1998 [3].

The University of Bristol team is working on multistatic ultrawideband (UWB) radar for breast cancer detection. Our radar system is based on a real (as opposed to synthetic) aperture antenna array. We have also developed a realistic 3D curved breast phantom with appropriate electrical properties. Moreover, our experimental system was built in such

a way that it can be used directly with real breast cancer patients (clinical trials have been recently commenced).

2. MEASUREMENT SETUP

We have developed a microwave radar for breast cancer detection, based on a curved hemispherical antenna array. In this paper, we present results obtained using a second-generation symmetrical antenna array. The new symmetrical antenna array, shown in Figure 1, uses a recently redesigned, smaller, stacked-patch antenna [4]. The array is formed around the lower part of a 78 mm radius sphere, in four rows of four antennas. Antennas are aligned in rows and columns; thus the array has two axes of symmetry.

During laboratory experiments, the array is first filled with a matching medium, the spherical skin phantom (2 mm thick) is placed in the correct position, and then we attach a tank to the top of the antenna array to finally fill it with a breast fat equivalent liquid [5] (the same as the matching medium). This setup represents truly a three-dimensional (3D) breast phantom. The chest wall is not considered in our experiments. The electrical properties of the tissue phantom are based on the published permittivity values for average human breast. At the frequency of 6 GHz, materials have

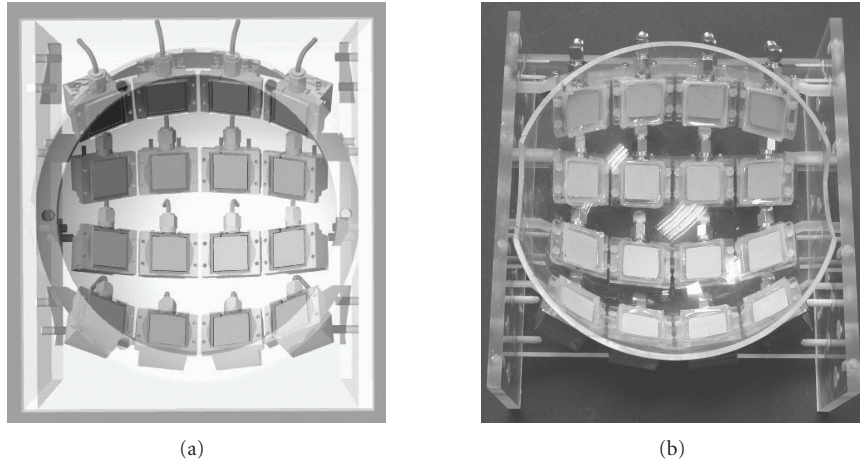


FIGURE 1: Symmetrical curved antenna array used in microwave radar for breast cancer detection: (a) CAD model, (b) photograph of the manufactured array. The array consists of sixteen UWB antennas populated on a section of hemisphere.

the following values. (a) Breast fat/matching medium has permittivity close to 10 and attenuation of 0.8 dB/cm; (b) skin phantom has permittivity of 30 and attenuation of 16 dB/cm; (c) tumour phantom has permittivity close to 50 and conductivity of 7 S/m. More details about our breast phantom can be found in [6].

The contrast between dielectric properties of breast fat and tumour phantom materials is around 1 : 5. Recently published data in [7], based on a large clinical study, suggest that the contrast between healthy and malignant breast tissues might also be lower. The lower contrast obviously poses a more challenging radar detection problem.

Our radar system operates in the multistatic mode. With sixteen antennas in the array, one hundred and twenty (120) independent radar measurements are recorded for processing (the monostatic measurement is not performed). Measurements are performed in the frequency domain between 3 and 10 GHz using a standard vector network analyser (VNA). All recorded radar signals are transformed into the time domain for further signal processing (described in Section 3).

3. FOCUSING ALGORITHM

3.1. Extraction of tumour response from measured radar data

The first step of signal processing deals with the extraction of the tumour response from the raw measured data. This process must be performed before equalisation and beamforming algorithms will be applied. When a monostatic synthetic aperture radar is used for breast cancer detection, tumour extraction aims at removing strong skin reflection from measured data. This is usually performed by simple subtraction from the averaged skin reflection signal (see [8]), or by more sophisticated algorithms as presented in [9].

The approach we use to extract the tumour response is different. In our multistatic real aperture array, the measured

response contains not only strong skin reflections, but also reflections from other mechanical parts of the array as well as antenna coupling signals. All these undesired signals are usually of greater amplitude than that of the tumour response. To subtract all unwanted signals, we physically rotate the antenna array around its center and perform a second radar measurement. This target displacement method is commonly used in radar cross-section measurements [10, 11] to subtract undesired signals.

Rotation gives us two sets of measured data, in which undesired signals such as antenna coupling or skin reflections are almost identical and appear at the same time position; therefore they can be eliminated. In contrast, a tumour response will appear at different time position in these two measured sets (unless it is on the axis of rotation). Applicability of this technique will depend on the homogeneity of the breast within a given angle defined by rotation. We therefore assume that within the angle of array rotation, (a) distance between antennas and skin remains unchanged, (b) skin properties and thickness are the same, and (c) normal breast tissue properties do not change. For more details about the performance of this tumour extraction technique, please refer to [12].

3.2. Preprocessing (equalisation)

Before applying the focusing algorithm, we have to perform a preprocessing step. This process aims at the equalisation of scattered tumour responses for different antenna pairs. Ideal preprocessing would result in all received pulses being of the same shape and amplitude, and perfectly time-aligned. In our preprocessing, the following steps are performed: (1) extraction of the tumour response from measured data (see [12]), (2) equalisation of tissue losses, and (3) equalisation of radial spread of the spherical wavefront. In the work reported herein for simplicity we do not account for the frequency dependence of the tissue losses nor for the frequency-dependent radiation patterns of the antennas.

3.3. Standard delay-and-sum algorithm

Delay-and-sum (DAS) beamforming is a basic and well-known method [13, 14]. First, we perform the preprocessing steps described above. Next, appropriate time-delays T_i for all received signals are computed. The time-delay T_i for a given transmitting and receiving antenna is calculated based on the antenna's position, position of the focal point $r = (x, y, z)$, as well as an estimate of average wave propagation speed, which in our case is simply assumed to be constant across the band.

During the focusing, the focal point moves from one position to another within the breast, resulting in spatial beamforming. At each location, all time-shifted responses are coherently summed and integrated. Integration is performed on the windowed signal, and the length of the integration window is chosen according to the system bandwidth. A three-dimensional (3D) map of scattered energy is formed in this way. The main advantage of the DAS algorithm is its simplicity, robustness, and short computation time.

Essentially, the scattered energy at the given focal point within the breast volume can be expressed as

$$F_e(x, y, z) = \int_0^\tau \left(\sum_{i=1}^M w_i(x, y, z) \cdot y_i(t - T_i(x, y, z)) \right)^2 dt, \quad (1)$$

where $M = N(N - 1)/2$ (N is the number of antennas in the array), w_i is the location-dependent weight calculated during preprocessing, y_i is the measured radar signal, and T_i is the time-delay. τ is the length of the integration window, chosen according to the system bandwidth. Due to the antenna effects and dispersion, the integration window we utilize following coherent summation is 50 percent longer than the duration of the synthetic input pulse and equals 0.55 nanosecond. We have investigated the dependence of the window length on focusing quality, and this value gave the best results.

3.4. Improved delay-and-sum algorithm

The improved DAS algorithm uses an additional weighting factor QF (quality factor), compared to the standard DAS. QF can be interpreted as a quality factor of the coherent focusing algorithm. It is calculated in three steps. Firstly, for each focal point, we plot a curve of energy collection during the coherent signal summation. An example of such a measured curve at a focal point containing a tumour response is presented in Figure 2.

Next, the energy collection curve is rescaled by normalising it to the standard deviation of energy, σ_e , for all radar signals used in the summation. Normalisation is actually performed using multiplication by $1/(1 + \sigma_e)$, since in the ideal case of equal energy in all (equalised) measured radar signals, $\sigma_e = 0$. This may be thought of as a heuristic scaling of the data to give greater weight to those signals that, following equalisation, more closely resemble the desired case of equal energy. The utility of this heuristic weighting is evident from the results presented in the following sections.

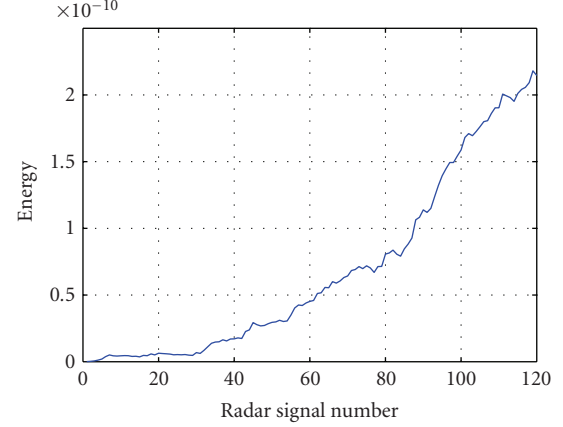


FIGURE 2: Example of the curve of energy collection (measured data).

In a last step, we estimate the coefficients of a second-order polynomial ($y = ax^2 + bx + c$), which is the least-square fit of the normalised curve of coherent energy collection. The choice of the second-order polynomial comes from the fact that a curve of energy collection during a perfect coherent signal summation would follow a quadratic curve. Then, we assume that $QF = a$. An order in which the signals are taken should not change the shape of the curve, assuming the perfect equalisation. In practise, due to a nonideal equalisation, the shape of the curve of energy collection will slightly depend on the order in which signals are summed. However, it has negligible effect on an a value since the final value of summed energy is constant; a is calculated using least-square fitting. Finally, the characteristic equation of the improved DAS algorithm is expressed as

$$F_e(x, y, z) = QF(x, y, z) \cdot \int_0^\tau \left(\sum_{i=1}^M w_i(x, y, z) \cdot y_i(t - T_i(x, y, z)) \right)^2 dt. \quad (2)$$

In the following section, we will present the experimental results of phantom tumours detection, and discuss the new DAS algorithm.

4. EXPERIMENTAL DETECTION RESULTS

This section presents the experimental results of tumour detection using our curved antenna array and 3D breast phantom. Focusing results for standard DAS algorithm are compared to those for the improved DAS, and differences between both algorithms are discussed. Results are presented for tumours of two different sizes located at different positions: (a) 10 mm spherical tumour located at position $P_T(x = 20, y = 20, z = -20)$, (b) 7 mm spherical tumour located at position $P_T(x = 20, y = 10, z = -10)$. All coordinates are quoted in millimeter.

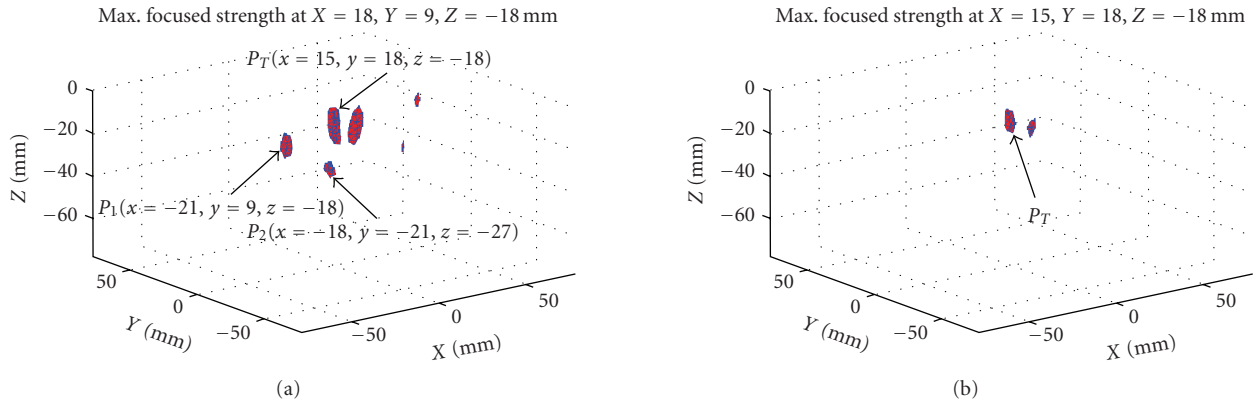


FIGURE 3: Detection results of a 10 mm spherical phantom tumour: (a) standard DAS, (b) improved DAS with $QF = a$. 3D figures present -3 dB contour map of scattered energy.

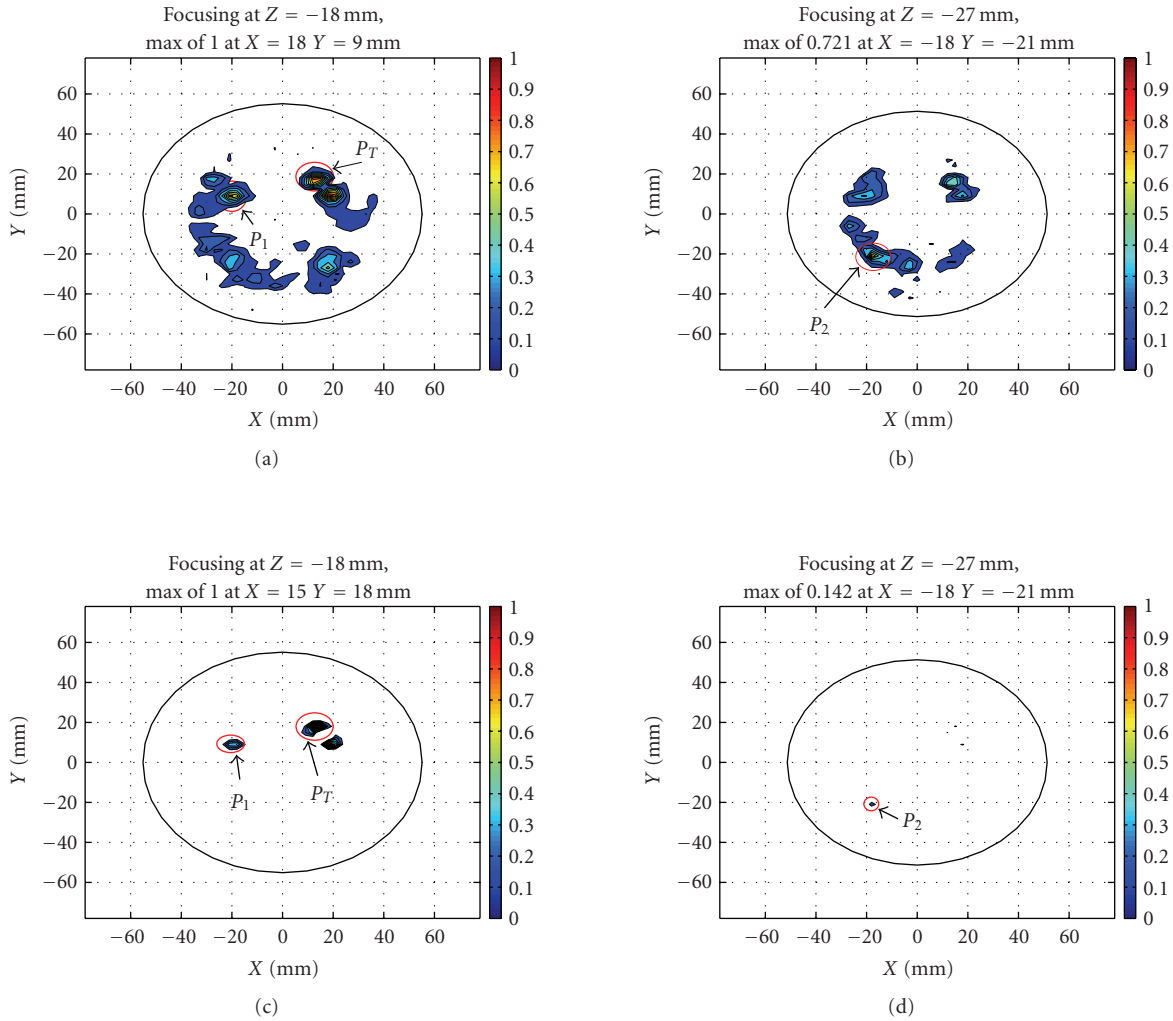


FIGURE 4: 2D focusing results for standard and improved DAS algorithms, for different horizontal planes along the z -axis: (a) standard DAS ($z = -18$), (b) standard DAS ($z = -27$), (c) improved DAS ($z = -18$), (d) improved DAS ($z = -27$). 2D contour plots show signal energy on a linear scale, normalised to the maximum in the 3D volume; values below 0.1 are rendered as white.

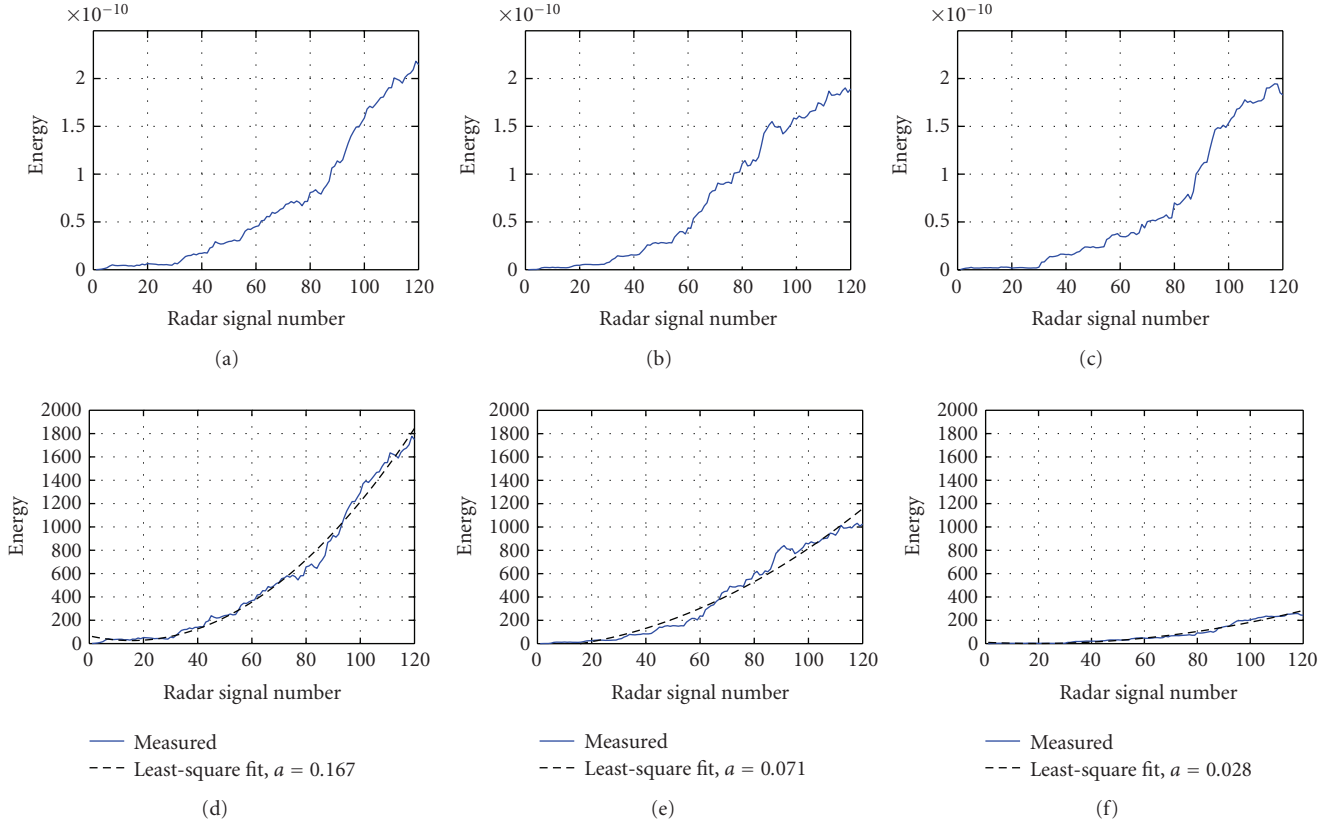


FIGURE 5: Curves of energy collection at focal points P_T , P_1 , and P_2 (see Figure 6(a)): (a) curve for P_T as in standard DAS, (b) curve for P_1 as in standard DAS, (c) curve for P_2 in standard DAS, (d) curve for P_T as in improved DAS together with the fitted polynomial, (e) curve for P_1 in the improved DAS together with the fitted polynomial, (f) curve for P_2 in the improved DAS together with the fitted polynomial.

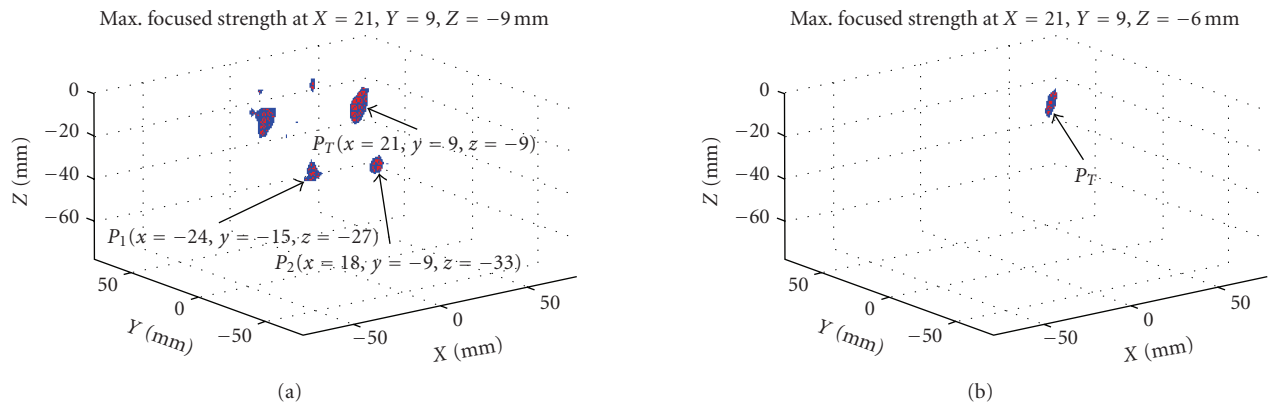


FIGURE 6: Detection results of a 7 mm spherical phantom tumour: (a) standard DAS, (b) improved DAS with $QF = a$. 3D figures present -3 dB contour map of scattered energy.

4.1. 10 mm spherical phantom tumour

In Figure 3, we present 3D focusing results for a 10 mm spherical phantom tumour located at the position $P_T(x = 20, y = 20, z = -20)$. Figures present -3 dB contour maps of scattered energy, when the focusing was performed using the standard DAS algorithm (Figure 3(a)) and the improved DAS algorithm (Figure 3(b)).

As we can see in Figure 3(a), there are several scatterers present in the image when focusing using standard DAS algorithm. The strongest scatterer within the entire 3D volume is located at position $P_T(x = 15, y = 18, z = -18)$, and it is associated with tumour response. In Figure 3, we have also indicated locations of two other strong scatterers located at positions $P_1(x = -21, y = 9, z = -18)$ and $P_2(x = -18, y = -21, z = -27)$. In Figures 4(a) and

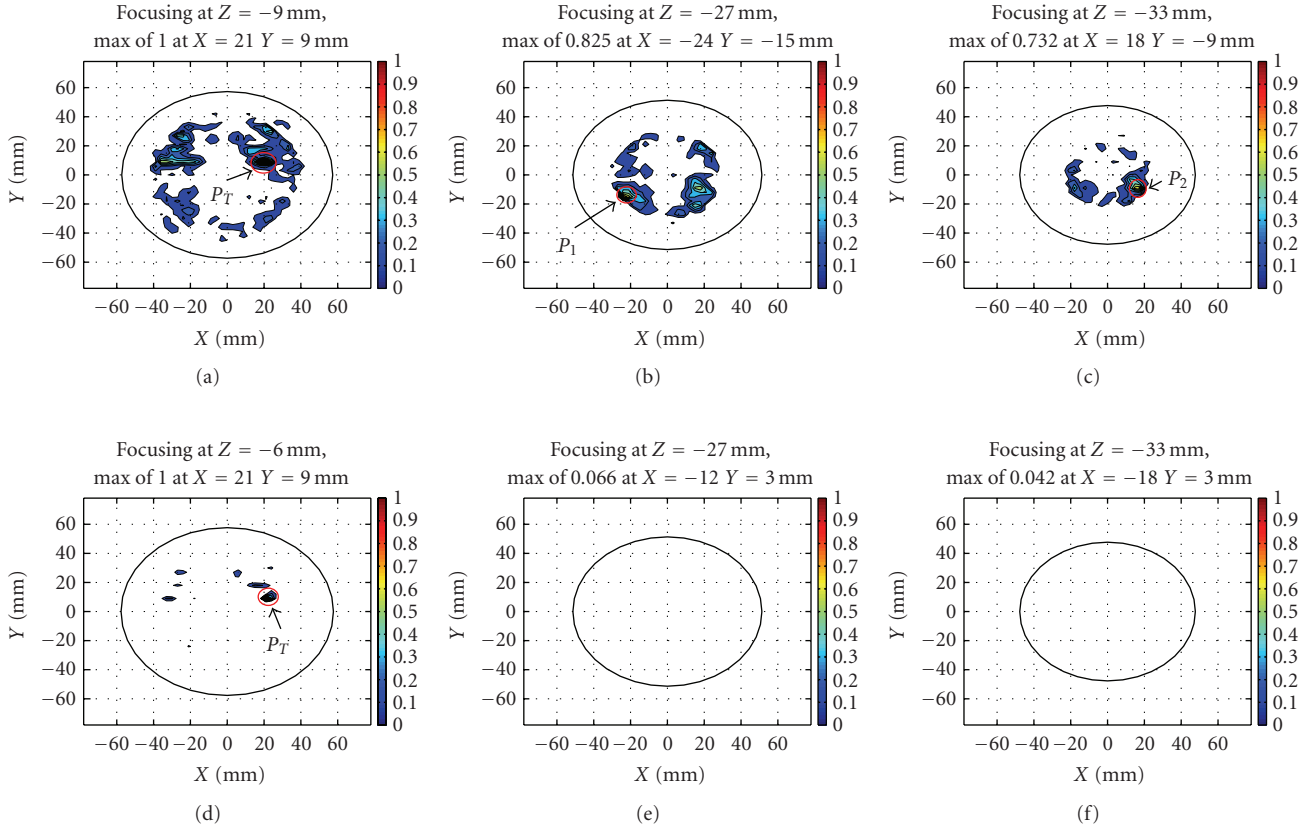


FIGURE 7: 2D focusing results for standard and improved DAS algorithms, for different horizontal planes along the z -axis: (a) standard DAS ($z = -9$), (b) standard DAS ($z = -27$), (c) standard DAS ($z = -33$), (d) improved DAS ($z = -6$), (e) improved DAS ($z = -27$), (f) improved DAS ($z = -33$). 2D contour plots show signal energy on a linear scale, normalised to the maximum in the 3D volume; values below 0.1 are rendered as white.

4(b), we present 2D focusing results for standard DAS on the horizontal planes (z -axis) containing the P_T , P_1 (both at $z = -18$), and P_2 ($z = -27$) signals associated with clutter. The 2D contour plots show signal energy on a linear scale, normalised to the maximum in the entire 3D volume (values below 0.1 are rendered as white). The skin location at each plane is presented as a black circle. From Figure 4(a), for the plane containing tumour we can relatively easily recognise the focused tumour response (P_T) and the nearby *twin* tumour response (at $x = 18$, $y = 9$; the *twin target* response is due to tumour extraction method—mechanical array rotation by 10 degrees). In the same figure, we can also see that the strong clutter at position P_1 and the weaker clutter (blue patches) at other positions arose from imperfect extraction of tumour response. Figure 4(b) presents the 2D focusing result through the plane ($z = -27$) containing strong clutter scatterer at P_2 .

Significantly better detection results were obtained using improved DAS algorithm presented herein. 3D and 2D focusing results for the improved DAS are presented in Figures 3(b) and 4(c)-4(d), respectively. The 3D contour map of scattered energy contains only the tumour response (P_T) and the twin tumour response. Unlike the image obtained using standard DAS, there are no other clutter scatterers visible. Signal-to-clutter ratio, defined as the ratio

between energy of the tumour response and the strongest clutter energy within a single 3D dataset, was improved from 1.25 dB for standard DAS to 3.9 dB for improved DAS (2.65 dB improvement).

The same improved performance is observed in the 2D results shown in Figures 4(c) and 4(d). In the horizontal plane containing P_T , the tumour response clearly stands out, and very little clutter exists in the image. In the plane containing P_2 , clutter is also significantly suppressed.

Results described above (Figures 3 and 4) have shown the improved tumour detection of the new DAS algorithm, which uses additional weight QF, compared to standard DAS. In what follows, we will analyse the improved DAS algorithm and explain why it provides better results. To do so, we will go through all steps of the new algorithm at the three focal points (P_T , P_1 , P_2) mentioned earlier in this section.

After extraction of the tumour response from measured data (by mechanical array rotation), resultant signals are being preprocessed and time-aligned. This initial step is identical for standard and improved DAS algorithms. Then, all pulsed signals (120 signals for our radar) are coherently summed. During this process, the curve of coherent energy collection is obtained, at each focal point within the focusing volume. This curve is presented in Figures 5(a)–5(c) for focal points P_T , P_1 , P_2 , respectively. The final value obtained after

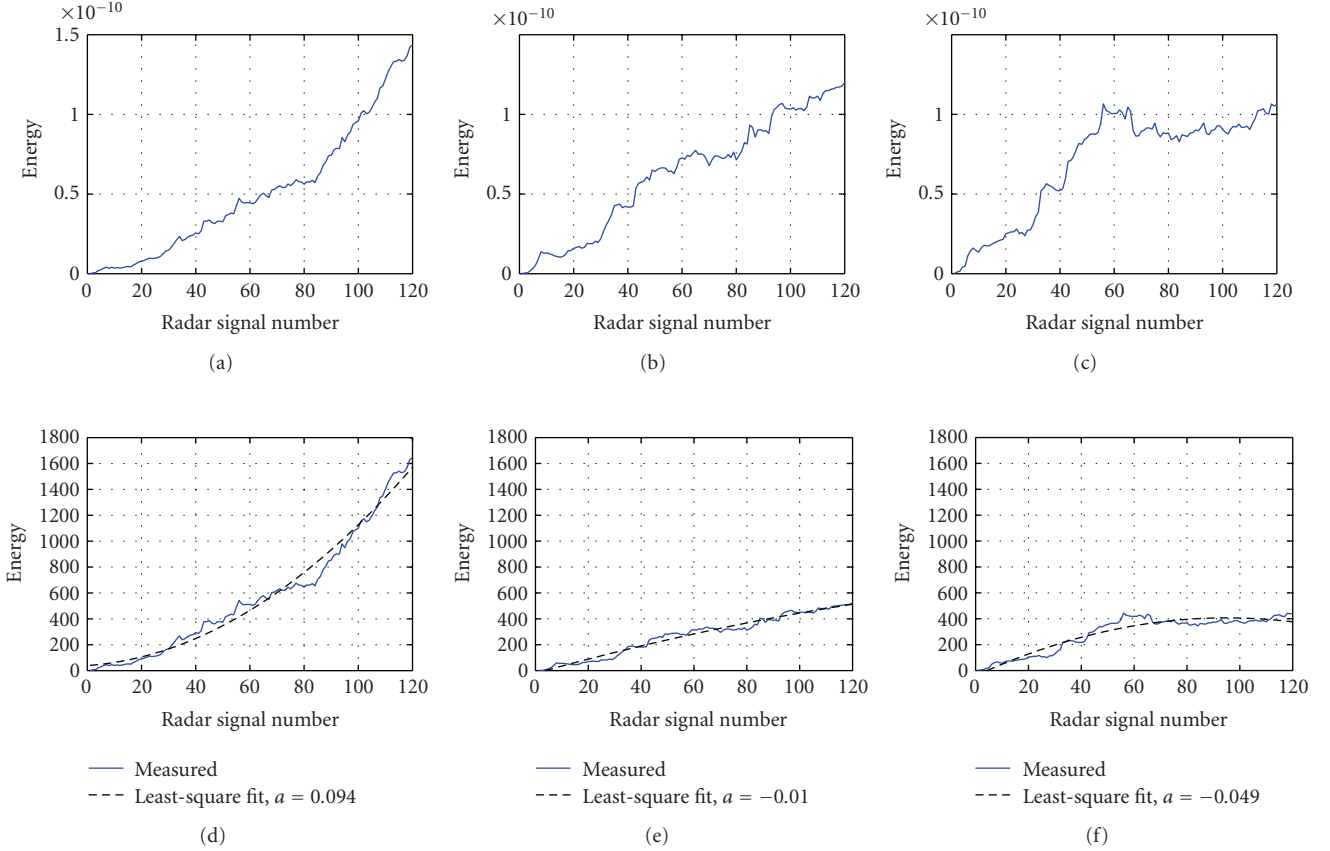


FIGURE 8: Curves of energy collection at focal points P_T , P_1 , and P_2 (see Figure 6(a)): (a) curve for P_T as in standard DAS, (b) curve for P_1 as in standard DAS, (c) curve for P_2 as in standard DAS, (d) curve for P_T as in improved DAS together with the fitted polynomial, (e) curve for P_1 in the improved DAS together with the fitted polynomial, (f) curve for P_2 in the improved DAS together with the fitted polynomial.

summation of all radar signals is equal to the focused energy F_e in standard DAS.

If we assume that the focused energy for tumour location using standard DAS algorithm is equal to unity $F_s(P_T) = 1$, focused energy values at focal points P_1 and P_2 equal $F_s(P_1) = 0.88$ and $F_s(P_2) = 0.85$. Next, in the improved DAS algorithm, we calculate the standard deviation of energy σ_e for all radar signals, and recalculate energy collection curves by normalising them to σ_e . The rationale to do so is based on the fact that after the initial preprocessing equalisation step, all radar signals should have similar energy.

We can see the rescaled (normalised) curves in Figures 5(d)–5(f) (solid blue curves) for locations P_T , P_1 , P_2 , respectively. We observe that after this normalisation the results have improved since the curves for P_1 , P_2 have significantly smaller amplitudes than for P_T . Since clutter signals cannot be thought of as being totally uncorrelated, we do not however simply use σ_e as the weight factor, but we apply additional criteria related to the coherent summation of radar signals as follows.

As known in the ideal coherent summation of scattered pulses, the energy collection curve should follow a parabola ($y = x^2$). Therefore, to check the “quality” of coherent addition of radar signals in our system, we perform a second-order polynomial ($y = ax^2 + bx + c$) fitting (in the least-

square sense) to the measured energy collection curves. This process is performed on the normalised curves. Results of polynomial fitting are shown in Figures 5(d)–5(f) (dashed black curves), and the constant a associated with x^2 equals $a = 0.167$ for P_T , $a = 0.071$ for P_1 , and $a = 0.028$ for P_2 . Then, assuming that $QF = a$ (see (2)), focused energy using improved DAS at our example points of interest is $F_s(P_T) = 1$, $F_s(P_1) = 0.38$, and $F_s(P_2) = 0.14$. The result of applying this process throughout the entire volume is shown in 3D and 2D by Figures 3 and 4, respectively.

4.2. 7 mm spherical phantom tumour

This example presents the detection of a smaller 7 mm spherical tumour phantom. In Figure 6, we present 3D focusing results for the 6 mm spherical phantom tumour located at the position $P_T(x = 20, y = 10, z = -10)$. Figures present -3 dB contour maps of scattered energy, when focusing was performed using the standard DAS algorithm (Figure 6(a)) and the improved DAS algorithm (Figure 6(b)).

As we can see in Figure 6(a), by using standard DAS algorithm there are multiple scatterers present in the image. As we did previously for the 10 mm tumour, again this time we concentrate the attention on three focal points: spherical

phantom tumour located at $P_T(x = 21, y = 9, z = -6)$, the strongest clutter scatterer at $P_1(x = -24, y = -15, z = -27)$, and another strong clutter at $P_2(x = 18, y = -9, z = -33)$. A significantly better image, with clearly visible tumour scatterer at P_T and no other clutter targets, is presented in Figure 6(b) for the improved DAS algorithm. Signal-to-clutter ratio was improved from 0.8 dB for standard DAS to 5.2 dB for improved DAS, providing 4.4 dB better performance using a proposed algorithm.

Looking at all 2D focused images (Figure 7) for standard DAS, we can observe that clutter strength generally increases closer to skin. This observation is confirmed when looking at locations of focal points investigated above. In our 3D breast phantom, the 2 mm skin layer has a radius $r_{\text{skin}} = 59$ mm. The true tumour response at P_T is located 35 mm away from the skin ($r_{P_T} = 24$ mm), the strongest clutter signal at P_1 is 20 mm away from the skin ($r_{P_1} = 39$ mm), and another strong clutter at P_2 is also 20 mm away from the skin ($r_{P_2} = 39$ mm). As we can see, all the strong clutter signals are located closer to skin than to the tumour.

In Figure 8, curves of coherent energy collection are presented for focal points P_T, P_1, P_2 . Plots associated with standard DAS algorithm are shown in Figures 8(a)–8(c) for focal points P_T, P_1, P_2 , respectively. The value obtained after summation of all radar signals is equal to the focused energy F_e in standard DAS. Next, in the improved DAS algorithm we calculate the standard deviation of energy σ_e for all radar signals, and recalculate energy collection curves by normalising them to σ_e . Resultant normalised curves for locations P_T, P_1 , and P_2 are depicted in Figures 8(d)–8(f) (solid blue curves), respectively.

We observe that, after normalisation, the curves for P_1, P_2 have significantly dropped compared to P_T , due to the higher values of standard deviation of the energy content of the radar signals. Next, we performed the second-order polynomial fitting on the normalised energy collection curves to obtain the weight factor $\text{QF} = a$. Results of polynomial fitting are shown as dashed black curve in Figures 8(d)–8(f). The constant a associated with x^2 equals $a = 0.094$ for P_T , $a = -0.01$ for P_1 , and $a = -0.049$ for P_2 . Interestingly, due to a noncoherent signal summation for focal points P_1 and P_2 , a has not only lower absolute value than for P_T , but has also negative sign. The focused energy F_e using improved DAS algorithm (as in (2)) will become negative for focal points, where $\text{QF} = a < 0$, additionally improving imaging results.

5. CONCLUSIONS

In this paper, we have presented a modified delay-and-sum (DAS) beamforming algorithm for breast cancer detection. The improved DAS algorithm uses an additional weight factor calculated at each focal point, to improve image quality. These weights essentially represent the quality of the preprocessing step and the coherent radar operation. Using measured data from a multistatic UWB radar system, we have presented experimental detection of 7 mm and 10 mm tumours in a phantom. We have shown that the proposed new DAS algorithm improves signal-to-clutter

ratio in focused images by 2.65 dB for 10 mm tumour, and by 4.4 dB for 7 mm tumour.

Further, it may be noted that this improvement in signal-to-clutter ratio is comparable to that achieved [12] by a much more complex data-adaptive algorithm based on robust Capon beamforming. Importantly, however, it requires significantly less (order-of-magnitude) computation time.

REFERENCES

- [1] E. C. Fear, P. M. Meaney, and M. A. Stuchly, "Microwaves for breast cancer detection?" *IEEE Potentials*, vol. 22, no. 1, pp. 12–18, 2003.
- [2] R. Bejnamin, "Synthetic, post-reception focusing in near-field radar," in *Proceedings of the EUREL International Conference on the Detection of Abandoned Land Mines: A Humanitarian Imperative Seeking a Technical Solution*, pp. 133–137, Edinburgh, UK, October 1996.
- [3] S. C. Hagness, A. Taflove, and J. E. Bridges, "Two-dimensional FDTD analysis of a pulsed microwave confocal system for breast cancer detection: fixed-focus and antenna-array sensors," *IEEE Transactions on Biomedical Engineering*, vol. 45, no. 12, pp. 1470–1479, 1998.
- [4] I. J. Craddock, M. Klemm, J. Leendertz, A. W. Preece, and R. Benjamin, "An improved hemispherical antenna array design for breast imaging," in *Proceedings of the 2nd European Conference on Antennas and Propagation (EuCAP '07)*, Edinburgh, UK, November 2007.
- [5] J. Leendertz, A. Preece, R. Nilavalan, I. J. Craddock, and R. Benjamin, "A liquid phantom medium for microwave breast imaging," in *Proceedings of the 6th International Congress of the European Bioelectromagnetics Association*, Budapest, Hungary, November 2003.
- [6] M. Klemm, I. J. Craddock, J. Leendertz, A. W. Preece, and R. Benjamin, "Breast cancer detection using symmetrical antenna array," in *Proceedings of the 2nd European Conference on Antennas and Propagation (EuCAP '07)*, pp. 1–5, Edinburgh, UK, November 2007.
- [7] M. Lazebnik, L. McCartney, D. Popovic, et al., "A large-scale study of the ultrawideband microwave dielectric properties of normal breast tissue obtained from reduction surgeries," *Physics in Medicine and Biology*, vol. 52, no. 10, pp. 2637–2656, 2007.
- [8] E. C. Fear, X. Li, S. C. Hagness, and M. A. Stuchly, "Confocal microwave imaging for breast cancer detection: localization of tumors in three dimensions," *IEEE Transactions on Biomedical Engineering*, vol. 49, no. 8, pp. 812–822, 2002.
- [9] E. J. Bond, X. Li, S. C. Hagness, and B. D. Van Veen, "Microwave imaging via space-time beamforming for early detection of breast cancer," *IEEE Transactions on Antennas and Propagation*, vol. 51, no. 8, pp. 1690–1705, 2003.
- [10] R. A. Marr, U. H. W. Lammers, T. B. Hansen, T. J. Tanigawa, and R. V. McGahan, "Bistatic RCS calculations from cylindrical near-field measurements—part II: experiments," *IEEE Transactions on Antennas and Propagation*, vol. 54, no. 12, pp. 3857–3864, 2006.
- [11] I. J. LaHaie and M. A. Blischke, "Mitigation of multipath and ground interactions in RCS measurements using a single target translation," in *Proceedings of the 23rd Annual Meeting of the Antenna Measurement Techniques Association (AMTA '01)*, pp. 411–416, Denver, Colo, USA, October 2001.
- [12] M. Klemm, I. J. Craddock, J. A. Leendertz, A. Preece, and R. Benjamin, "Breast cancer detection using a hemi-spherical

antenna array—experimental results,” submitted to *IEEE Transactions on Antennas and Propagation*.

- [13] W. Shao, B. Zhou, Z. Zheng, and G. Wang, “UWB microwave imaging for breast tumor detection in inhomogeneous tissue,” in *Proceedings of the 27th IEEE Annual International Conference of the Engineering in Medicine and Biology Society (EMBS '05)*, pp. 1496–1499, Shanghai, China, September 2005.
- [14] Z. Wang, J. Li, and R. Wu, “Time-delay- and time-reversal-based robust Capon beamformers for ultrasound imaging,” *IEEE Transactions on Medical Imaging*, vol. 24, no. 10, pp. 1308–1322, 2005.



Hindawi

Submit your manuscripts at
<http://www.hindawi.com>

